Efficient correction of wavefront inhomogeneities in X-ray holographic nanotomography by random sample displacement

Maxime Hubert, Alexandra Pacureanu, Cyril Guilloud, Yang Yang, Julio C. da Silva, Jerome Laurencin, Florence Lefebvre-Joud, Peter Cloetens

To cite this version:

Maxime Hubert, Alexandra Pacureanu, Cyril Guilloud, Yang Yang, Julio C. da Silva, et al.. Efficient correction of wavefront inhomogeneities in X-ray holographic nanotomography by random sample displacement. Applied Physics Letters, 2018, 112 (20), pp.203704-1-203704-5. ⟨10.1063/1.5026462⟩. ⟨hal-02976439⟩

HAL Id: hal-02976439
https://hal.science/hal-02976439v1

Submitted on 23 Oct 2020

APPLIED PHYSICS LETTERS **112**, 203704 (2018)

Efficient correction of wavefront inhomogeneities in X-ray holographic nanotomography by random sample displacement

Maxime Hubert,[1,2] Alexandra Pacureanu,[1] Cyril Guilloud,[1] Yang Yang,[1] Julio C. da Silva,[1] Jerome Laurencin,[2] Florence Lefebvre-Joud,[2] and Peter Cloetens[1]
[1]*European Synchrotron Radiation Facility, 38000 Grenoble, France*
[2]*University Grenoble Alpes-CEA/LITEN, 38054 Grenoble, France*

(Received 20 February 2018; accepted 30 April 2018; published online 18 May 2018)

In X-ray tomography, ring-shaped artifacts present in the reconstructed slices are an inherent problem degrading the global image quality and hindering the extraction of quantitative information. To overcome this issue, we propose a strategy for suppression of ring artifacts originating from the coherent mixing of the incident wave and the object. We discuss the limits of validity of the empty beam correction in the framework of a simple formalism. We then deduce a correction method based on two-dimensional random sample displacement, with minimal cost in terms of spatial resolution, acquisition, and processing time. The method is demonstrated on bone tissue and on a hydrogen electrode of a ceramic-metallic solid oxide cell. Compared to the standard empty beam correction, we obtain high quality nanotomography images revealing detailed object features. The resulting absence of artifacts allows straightforward segmentation and posterior quantification of the data.
https://doi.org/10.1063/1.5026462

X-ray nanotomography is a powerful non-destructive imaging technique, which provides a volume reconstruction of an object from a set of projections acquired at different rotational angles. It is instrumental in many scientific domains such as biomedicine, microelectronics, materials science or energy.[1–6] The generated three-dimensional (3D) data are used to reveal the essential properties of the samples. The extraction of knowledge from the images is often hindered by ring shaped artifacts appearing on the reconstructed transverse slices, an inherent problem in tomography. They can have different origins such as imperfections of the X-ray optics or a non-uniform pixel response of the detector. The parasitic signal is localized on the same pixel of all angular projections, thus giving rise to a ring in the transverse cross-sections of the 3D data set.[7–9]

The standard approach to reduce artifacts is the "empty beam correction." It consists of dividing the observed image of the sample $I_{\text{mixed}}(x, y)$ by an image obtained under the same conditions without the sample $I_{\text{empty}}(x, y)$ to extract the ratio $I_{\text{mixed}}/I_{\text{empty}}$ which is assumed to depend only on the object. This correction reaches its limit of validity when the X-ray beam is polychromatic,[7,10] when the point-spread-function of the detector plays a significant role[8] or when there is a strong coherent mixing of the incoming wavefront and the object.[11,12] Two main methods have been widely developed to tackle the residual ring artifacts: (i) software-based methods relying on image processing after data acquisition and (ii) hardware-based methods consisting in moving the detector or the sample during the scan. For the software-based methods, several algorithms have been proposed to remove the ring artifacts either from the sinograms[9,13–15] or from the reconstructed slices.[16–20] These approaches are powerful but they require extra processing time and manual intervention. Moreover, the artifacts and the real object features are not perfectly separable what degrades the spatial resolution and contrast in the final images. For the hardware-based methods, thanks to the displacement of the detector or the sample, the faulty signal provoking the artifacts is not always localized on the same pixel during the recording of the projections.[21–23] Besides the need for accurate motion control, no complex additional processing is necessary after the acquisition.

In the case of partially coherent image formation, the empty beam correction assumes the following approximation:

$$\frac{I_{\text{mixed}}}{I_{\text{empty}}} = \frac{|D_z(P.O)|^2}{|D_z(P)|^2} \simeq |D_z(O)|^2 = I_{\text{obj}}, \tag{1}$$

where I_{obj} is the desired image of the object in the case of a homogeneous illumination. D_z denotes the Fresnel propagator at an effective propagation distance z for the object O or the probe P at the sample position. The propagator formalism can be applied to absorption tomography ($z = 0$), propagation based phase contrast tomography and full-field transmission tomography using lenses with defocusing as the only optical aberration. Powerful near-field ptychography techniques have been proposed to reconstruct the probe in parallel with the object to improve the image quality.[24–26] Nevertheless, they require long acquisition times at multiple lateral sample positions for each angle and the data analysis is computationally intensive. An exhaustive, but complex validity condition of the empty beam correction has been proposed,[12] which essentially states that the high frequency domain will be mostly affected when the modulations of the probe and object are large. Here, we formulate a simpler model to discuss the validity of the empty beam correction and propose a pragmatic solution based on random sample displacement to average out the artifacts. Assuming weak defocusing conditions,[27] the propagator can be linearized to yield the following expression for the ratio $I_{\mathrm{mixed}}/I_{\mathrm{empty}}$:

$$\frac{I_{\mathrm{mixed}}}{I_{\mathrm{empty}}} \simeq I_{\mathrm{obj}} - \frac{\lambda z}{\pi} M_O^2 \left[\nabla \ln(M_P) \nabla \varphi_O + \nabla \ln(M_O) \nabla \varphi_P\right], \quad (2)$$

where λ is the X-ray wavelength, $M_{O,P}$ and $\varphi_{O,P}$ are the amplitude and phase of the object O and the probe P, written in the Euler representation as $O = M_O \exp(i\varphi_O)$ and $P = M_P \exp(i\varphi_P)$, respectively. The second, parasitic term, shows that the phase of the object is coupled to the amplitude of the probe and vice versa. Thus, the empty beam correction fails even in the first order, at small defocus, when the amplitude and the phase gradients of object and probe are large. Our method is based on displacing randomly the sample orthogonally to the incoming beam between two successive angles of the tomographic scan. By re-aligning the projections with respect to the object during the data processing, the object information is correctly superimposed while the gradients of the amplitude and the phase of the probe, contained in the second term of Eq. (2), are smeared out.

The proposed method is routinely used for holographic nanotomography[28] at the Nano-Imaging beamline ID16A of the European Synchrotron Radiation Facility (ESRF). The X-ray beam produced by an undulator is focused by Kirkpatrick-Baez mirrors (KB)[29,30] located 185 m downstream the source. The KB mirrors are specifically adapted to the X-ray beam energies available on the beamline (17 and 33.6 keV).[31] The projections are recorded over 180° at four different focus-sample distances (Fig. 1) using a FReLoN CCD based detector placed at a constant distance from the focal plane during the experiment. The main principle of the modified data acquisition process is illustrated in Fig. 1.

The choice of the random displacement range is based on several factors. The speed of the piezo stages is considered to minimize the overhead in terms of scan duration. Another factor is the characteristic size of the beam features perturbing the 3D reconstructions, which is about 10 pixels wide in our case. The dominant object features are expected to be of the order of the first Fresnel zone $\sqrt{\lambda z}$. For a pixel size of 25 nm, the fringe spacing is about 34 pixels and 24 pixels at 17 keV and 33.6 keV, respectively (see supplementary material). As a compromise, we chose to move the sample randomly with equal probability in the range $[-r_{\mathrm{rand}}/2, r_{\mathrm{rand}}/2]$, with $r_{\mathrm{rand}} = 25$ pixels in the x and y directions for pixel sizes below 100 nm. For larger pixel sizes, the displacement range is usually limited to $r_{\mathrm{rand}} = 10$ pixels as the motor displacement significantly impacts the scan duration. To save time, the lateral movement with the piezo stages is synchronized with the incremental rotation. It should be noted that the random displacement approach is not compatible with a continuous tomography scan, a step-by-step acquisition is needed. Although this procedure is slower, it guarantees a high stability of the sample at each angle, a prerequisite for achieving high spatial resolution in the reconstruction. The exact positions of the sample for each angle and distance are stored and used during the phase retrieval procedure to align the projections amongst themselves by applying an opposite displacement. The obtained phase maps are thus aligned and no additional processing is needed. The 3D volume is finally reconstructed by Filtered Back Projection[32] using the ESRF software PyHST2.[33]

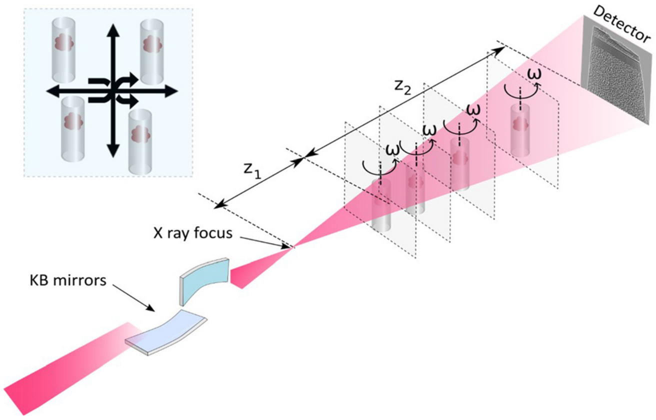

FIG. 1. Schematic representation of the experimental setup for X-ray holographic nanotomography at the ID16A beamline of the ESRF. Tomography scans are acquired at multiple focus-sample distances z_1. As illustrated in the inset, the sample is randomly displaced in each plane orthogonal to the X-ray propagation direction during the tomography scans.

In Fig. 2, we illustrate the method on a bone tissue sample. Figure 2(a) shows a raw projection I_{mixed}, mixing the probe and object information. Figure 2(c) displays the result of the standard correction by the empty beam I_{empty} shown in Fig. 2(b) as described by Eq. (1). We readily notice the remaining strong residues from the probe, especially in the bottom of the image where the phase gradient of the object ($\nabla \varphi_O$) is large due to a thicker region of the sample. Consequently, strong artifacts appear in the reconstructed tomographic slice [Fig. 2(d)]. These artifacts are no longer present on the reconstructed slice shown in Fig. 2(e) obtained using the random sample displacement process. The line profiles across the reconstructed density show that the canaliculi can be distinguished only in the case of the random sample displacement. Subtle gray-level variations observed in Fig. 2(e), demonstrate a higher sensitivity to density changes across the bone micro-pillar. Supplementary material shows the superior efficiency of applying 2D sample displacements in the plane orthogonal to the beam instead of 1D, horizontal or vertical displacements, as already proposed in the literature.[22]

The method is further demonstrated on a Solid Oxide Cell (SOC) electrode. This sample consists of a porous ceramic-metallic composite made of Nickel and Yttria stabilized Zirconia (Ni-YSZ). The reconstruction is challenging due to the complex microstructure and the strongly absorbing materials which, despite the high beam energy of 33.6 keV, impact the holographic phase retrieval. An empty-beam image I_{empty} is shown in Fig. 3(b). Strong contrast due to the KB mirror imperfections can be observed. These inhomogeneities mix with the sample in projection I_{mixed} shown in Fig. 3(a). The effect of this mixing is directly visible in the 3D reconstruction after phase retrieval despite the empty beam correction. Figure 3(c) shows a slice extracted from a 3D volume obtained using the standard acquisition and reconstruction process. Strong ring-like artifacts are apparent in the middle of the slice. They are not continuous like the usual rings and their size is similar to the sample features and to the wavefront inhomogeneities. The corresponding histogram [Fig. 3(e)] shows that the segmentation of the

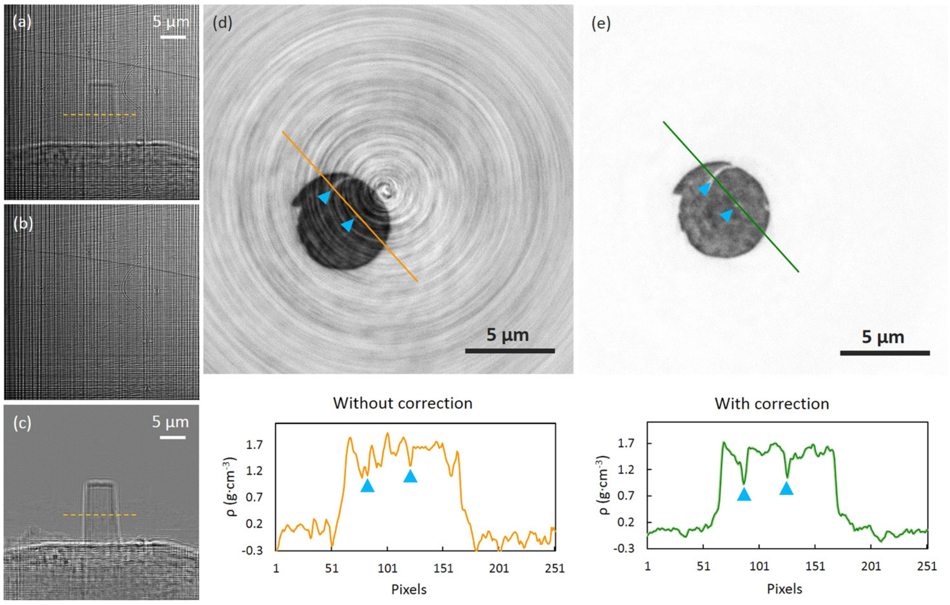

FIG. 2. Illustration of the object-probe mixing and of the correction obtained by random sample displacement using a bone tissue sample. Panels (a)–(c) Show the raw projection I_{mixed} (a), the projection without sample I_{empty} (b), and the empty beam corrected projection $I_{\mathrm{mixed}}/I_{\mathrm{empty}}$ (c). The dotted lines mark the position of the reconstructed cross-section shown in panels (d) and (e). The pixel size in the projections is 16 nm and the field of view is 32 μm. (d) Without random displacement, the reconstructed slice (top) and a profile plot of the density measured along the marked line (bottom) show that the artifacts hamper the distinction between sample structures (nano-porosities known as canaliculi highlighted by arrows) and the ring-shaped noise. (e) With the random displacement, the artifacts are efficiently removed and fine structures inside the sample are revealed. The voxel size in the tomography slices is 50 nm.

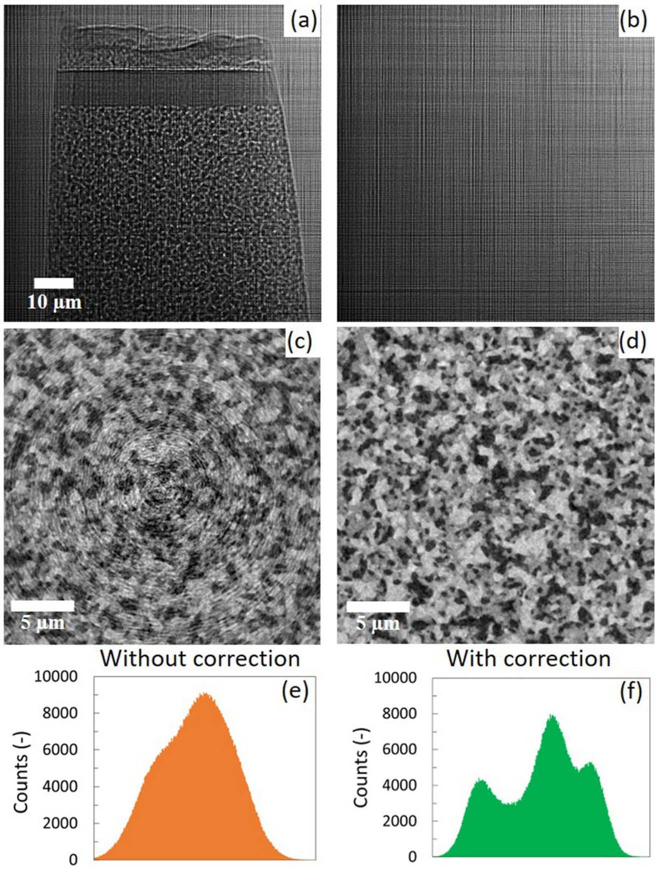

FIG. 3. Illustration of random displacement process with a SOC sample. Raw projection of the observed object I_{mixed} (a) and the image without sample I_{empty} (b). Slices extracted from the 3D volume and their associated histograms are shown for a reconstruction obtained without random displacement (c) and (e) and a volume obtained with the random displacement process (d) and (f). (Black = porosity, grey = YSZ, white = Ni, and voxel size = 25 nm).

three phases is unfeasible in this volume. Conversely, the slice [Fig. 3(d)] extracted from the reconstruction obtained with the random displacement process is free of artifacts. The segmentation of the three different phases is facilitated given that three peaks are clearly visible in the image histogram from Fig. 3(f). The striking improvement of the image quality confirms that our interpretation of the origin of the artifacts is correct and that the implemented experimental solution is highly efficient.

We have evaluated the possible undesirable effect of the random displacement process on the spatial resolution. The exact compensation of the random motion has been verified by calculating the small horizontal and vertical misalignment, named jitter, between the aligned projections and the forward projections, calculated from the reconstructed 3D volume using PyHST2. The jitter is calculated using cross correlation and shown in Fig. 4. A higher jitter amplitude is observed in the data obtained with the random displacement [Fig. 4(a)] compared to the data acquired without displacement [Fig. 4(b)]. The full width at half maximum (FWHM) of the jitter distribution is 5 nm in horizontal and 2 nm in vertical with the random displacement. The spatial resolution has been estimated by fitting a hyperbolic tangent function on the edge profile. A value of about 50 nm was deduced for the FWHM of the line spread function [Fig. 4(c)], comparable to the resolution previously obtained on similar samples.[34]

The quality of the reconstructed image obtained with the random motion method allows each phase to be segmented and quantified using protocols described in literature.[35,36] The microstructural properties of a porous Ni-YSZ electrode are extracted from a volume of $27.5 \times 27.5 \times 27.5\ \mu m^3$ with a 25 nm voxel size and summarized in Table I. The measured volume fraction agrees well with the value obtained by scanning electron microscopy and the manufacturer specifications.

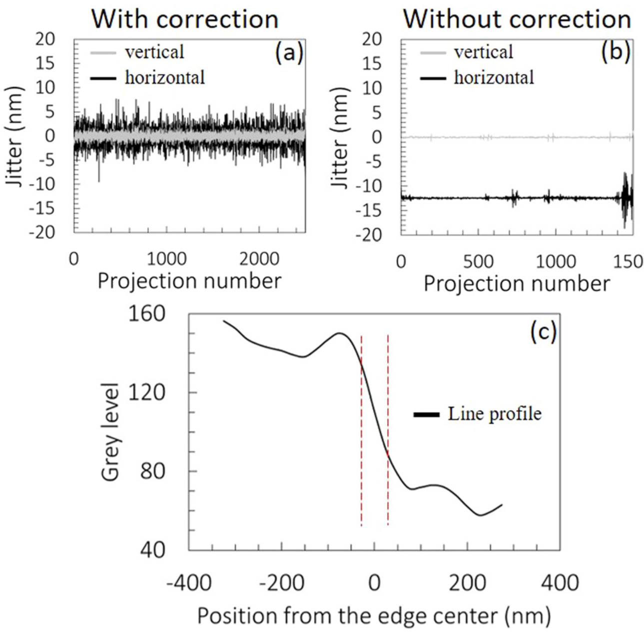

FIG. 4. Effect of the random displacement process on the spatial resolution. Horizontal (black) and vertical (gray) jitter for the sample scanned with (a) and without (b) the random displacement process. (c) An edge line profile through a pore-YSZ boundary for spatial resolution measurement.

The other properties are consistent with data from the literature on a similar electrode.[36–38] The Representative Volume Element (RVE) size, which is different according to the microstructure and the analyzed properties,[36,39–41] has been checked by looking at the evolution of the pore volume fraction as a function of the analyzed volume size. For this Ni-YSZ porous electrode, the RVE is around 15 × 15 × 15 μm^3 what is consistent with the characteristic size of porosity and the rule proposed in Harris *et al.*[39,40] The analyzed volume is larger than the RVE, thus the uncertainty in the computed microstructural parameters is expected to be low.

We have demonstrated here that the proposed 2D random sample displacement process efficiently removes artifacts caused by the incoming wavefront inhomogeneities in tomographic reconstructions. The image quality was greatly improved without impacting the spatial resolution and the acquisition duration, provided that a step-by-step procedure is used with precise motion control. The strength of the method was illustrated qualitatively and quantitatively on a bone micro-pillar and a SOC electrode with a complex microstructure. The procedure was supported by a simple mathematical model of the empty beam correction. In brief, we proposed here a simple solution to one of the most disturbing artifacts in tomographic reconstructions: the ring artifacts. In addition, we provided an analytical expression of the mixing of probe and object which serves as a basis for further interpretation of other phase contrast methods and of aspects of the near-field ptychography techniques.

TABLE I. Electrode microstructural parameters of a fresh Ni-YSZ electrode. The data reported in this table has been calculated on the percolated phases of the 3D volume obtained with the random displacement process.

Properties	Pores	YSZ	Ni
Percolated volume fraction (−)	0.280 ± 0.014	0.436 ± 0.003	0.262 ± 0.013
Mean particle diameter (μm)[a]	0.96 ± 0.06	0.60 ± 0.00	1.01 ± 0.03
Specific surface area (μm^{-1})	2.48 ± 0.07	3.62 ± 0.03	2.09 ± 0.09
Tortuosity factor (−)	8.46	2.27	7.45
Active triple phase boundary length density (μm^{-2})		4.75 ± 0.08	

[a] Mean phase diameter determined with the covariance function.

See supplementary material which provides details on the choice of the random displacement range and illustrates the effect of 1D, vertical or horizontal, versus 2D random sample displacement.

The authors thank Jean-Pierre Guigay for the fruitful discussions. The authors are grateful to Professor Philippe Zysset and to Dr. Uwe Wolfram for making available the bone sample.

[1] P. J. Withers, Mater. Today **10**, 26 (2007).
[2] S.-A. Zhou and A. Brahme, Phys. Med. **24**, 129 (2008).
[3] J. Bertheau, P. Bleuet, F. Hodaj, P. Cloetens, N. Martin, J. Charbonnier, and N. Hotellier, Microelectron. Eng. **113**, 123 (2014).
[4] M. Holt, R. Harder, R. Winarski, and V. Rose, Annu. Rev. Mater. Res. **43**, 183 (2013).
[5] Y. Liu, F. Meirer, C. M. Krest, S. Webb, and B. M. Weckhuysen, Nat. Commun. **7**, 12634 (2016).
[6] A. Cuesta, A. G. De la Torre, I. Santacruz, P. Trtik, J. C. da Silva, A. Diaz, M. Holler, and M. A. Aranda, J. Phys. Chem. C **121**, 3044 (2017).
[7] R. A. Ketcham and W. D. Carlson, Comput. Geosci. **27**, 381 (2001).
[8] F. P. Vidal, J. M. Létang, G. Peix, and P. Cloetens, Nucl. Instrum. Methods Phys. Res. Sect. B **234**, 333 (2005).
[9] M. Boin and A. Haibel, Opt. Express **14**, 12071 (2006).
[10] J. Jakubek, Nucl. Instrum. Methods Phys. Res. Sect. A **576**, 223 (2007).
[11] J. Hagemann, A.-L. Robisch, D. Luke, C. Homann, T. Hohage, P. Cloetens, H. Suhonen, and T. Salditt, Opt. Express **22**, 11552 (2014).
[12] C. Homann, T. Hohage, J. Hagemann, A.-L. Robisch, and T. Salditt, Phys. Rev. A **91**, 013821 (2015).
[13] C. Raven, Rev. Sci. Instrum. **69**, 2978 (1998).
[14] M. Yousuf and M. Asaduzzaman, J. Sci. Res. **2**, 37 (2010).
[15] S. Rashid, S. Y. Lee, and M. K. Hasan, EURASIP J. Adv. Signal Process. **2012**, 93 (2012).
[16] J. Sijbers and A. Postnov, Phys. Med. Biol. **49**, N247 (2004).
[17] Y. Kyriakou, D. Prell, and W. A. Kalender, Phys. Med. Biol. **54**, N385 (2009).
[18] A. Lyckegaard, G. Johnson, and P. Tafforeau, Int. J. Tomogr. Stat. **18**, 1 (2011), available at http://ceser.in/ceserp/index.php/ijts/article/view/205.
[19] F. Brun, A. Accardo, G. Kourousias, D. Dreossi, and R. Pugliese, in *2013 8th International Symposium on Image and Signal Processing and Analysis (ISPA)* (IEEE, 2013), pp. 672–676.
[20] D. Jha, H. O. Sørensen, S. Dobberschütz, R. Feidenhans'l, and S. L. S. Stipp, Appl. Phys. Lett. **105**, 143107 (2014).
[21] G. Davis and J. Elliott, Nucl. Instrum. Methods Phys. Res. Sect. A **394**, 157 (1997).
[22] P. Jenneson, W. Gilboy, E. Morton, and P. Gregory, Appl. Radiat. Isot. **58**, 177 (2003).
[23] Y. Zhu, M. Zhao, H. Li, and P. Zhang, Med. Phys. **40**, 031114 (2013).
[24] M. Stockmar, P. Cloetens, I. Zanette, B. Enders, M. Dierolf, F. Pfeiffer, and P. Thibault, Sci. Rep. **3**, 1927 (2013).
[25] A.-L. Robisch, J. Wallentin, A. Pacureanu, P. Cloetens, and T. Salditt, Opt. Lett. **41**, 5519 (2016).
[26] J. Hagemann, A.-L. Robisch, M. Osterhoff, and T. Salditt, J. Synchrotron Radiat. **24**, 498 (2017).
[27] J. M. Cowley, *Diffraction Physics*, 2nd ed. (North-Holland Publ. Co., Amsterdam, Oxford, 1975, 1984), p. 60.
[28] R. Mokso, P. Cloetens, E. Maire, W. Ludwig, and J.-Y. Buffière, Appl. Phys. Lett. **90**, 144104 (2007).
[29] P. Kirkpatrick and A. V. Baez, JOSA **38**, 766 (1948).
[30] J. C. da Silva, A. Pacureanu, Y. Yang, S. Bohic, C. Morawe, R. Barrett, and P. Cloetens, Optica **4**, 492 (2017).

[31] C. Morawe, R. Barrett, P. Cloetens, B. Lantelme, J.-C. Peffen, and A. Vivo, Proc. SPIE **9588**, 958803 (2015).

[32] R. N. Bracewell and A. C. Riddle, Astrophys. J. **150**, 427 (1967).

[33] A. Mirone, E. Brun, E. Gouillart, P. Tafforeau, and J. Kieffer, Nucl. Instrum. Methods Phys. Res. Sect. B **324**, 41 (2014).

[34] M. Hubert, J. Laurencin, P. Cloetens, J. C. da Silva, F. Lefebvre-Joud, P. Bleuet, A. Nakajo, and E. Siebert, Solid State Ionics **294**, 90 (2016).

[35] J. Villanova, J. Laurencin, P. Cloetens, P. Bleuet, G. Delette, H. Suhonen, and F. Usseglio-Viretta, J. Power Sources **243**, 841 (2013).

[36] F. Usseglio-Viretta, J. Laurencin, G. Delette, J. Villanova, P. Cloetens, and D. Leguillon, J. Power Sources **256**, 394 (2014).

[37] A. Nakajo, A. Cocco, M. DeGostin, A. Peracchio, B. Cassenti, M. Cantoni, J. Van herle, and W. Chiu, J. Power Sources **325**, 786 (2016).

[38] G. Brus, H. Iwai, A. Sciazko, M. Saito, H. Yoshida, and J. S. Szmyd, J. Power Sources **288**, 199 (2015).

[39] W. M. Harris and W. K. Chiu, J. Power Sources **282**, 552 (2015).

[40] W. M. Harris and W. K. Chiu, J. Power Sources **282**, 622 (2015).

[41] J. Laurencin, R. Quey, G. Delette, H. Suhonen, P. Cloetens, and P. Bleuet, J. Power Sources **198**, 182 (2012).